RSC Advances

PAPER

View Article Online
View Journal | View Issue

Cite this: *RSC Adv.*, 2024, **14**, 26775

Electrophoretic deposition of polyvinyl alcohol, C–H NRs along with moringa on an SS substrate for orthopedic implant applications

Esha Ghazanfar,[a] Mohsin Ali Marwat, †*[a] Syeda Ammara Batool,[b] Areeb Anwar,[c] Syed Muhammad Abdullah,[a] Zia Ud Din,[a] Muhammad Humayun,[d] Mohamed Bououdina,[d] Al-Badrawy Abo-Elnasr [e] and Hafiz Tauqeer Ali[e]

Metals are commonly used in bone implants due to their durability and load-bearing capabilities, yet they often suffer from biofilm growth and corrosion. To overcome these challenges, implants with enhanced biocompatibility, bioactivity, and antimicrobial properties are preferred. Stainless steel (SS) implants are widely favored in orthopedics for their mechanical strength and cost-effectiveness. To address the issues related to SS implants, we developed composite coatings using synthetic biopolymer polyvinyl alcohol (PVA), calcium hydrate (C–H) nanorods for improved bioactivity and antibacterial properties, and *Moringa oleifera* to enhance osteogenic induction. These coatings were deposited on 316L SS through electrophoretic deposition (EPD), providing protection against body fluids and enhancing the corrosion resistance of the SS. X-ray diffraction (XRD) confirmed the presence of the desired tobermorite crystal structure, while scanning electron microscopy (SEM) revealed nanorod-like C–H structures, a film thickness of 29 microns, and a hedgehog-like morphology in the composite particles. The coated sample demonstrated a contact angle of 64°, optimal for protein attachment and cellular uptake. Additionally, the coating exhibited strong adhesion with less than 5% damage observed in cross-cut hatch testing and appropriate surface roughness for protein attachment. Differential Scanning Calorimetry (DSC) and thermogravimetric analysis (TGA) assessed the thermal response of the materials. The coating also showed antibacterial activity against both Gram-negative and Gram-positive bacteria. Furthermore, the sample exhibited rapid bioactivity by forming a hydroxyapatite (HA) layer within 24 hours, with 35.4% degradability within 24 hours and 44.5% within 48 hours. These findings confirm that the composite film enhances the biocompatibility, bioactivity, and antibacterial properties of SS orthopedic implants in a cost-effective manner.

Received 28th May 2024
Accepted 17th August 2024

DOI: 10.1039/d4ra03931a

rsc.li/rsc-advances

1. Introduction

Orthopedic implants play an important role in restoring mobility and improving the quality of life for millions of individuals worldwide suffering from bone defects or traumatic injuries. Furthermore, the market for orthopedic implants worldwide was valued at USD 25.2 billion in 2024 and is projected to grow at a 3.7% annual pace through 2030.[1] Sometimes we need a permanent solution but sometimes we need a temporary implant to support bone regeneration.[2] However, the long-term success of orthopedic implants depends upon their mechanical integrity, biocompatibility, and corrosion resistance in the human body's harsh physiological environment.[3] Implant material selection plays a vital role in ensuring the success of surgical intervention. Many materials are available, but 316L SS is a prominent choice for orthopedic implants due to its cost-effectiveness, exceptional mechanical properties, biocompatibility, and corrosion resistance.[4] 316L SS based on the composition of iron, molybdenum, chromium, and nickel is an effective choice for orthopedic applications with exceptional mechanical strength, fatigue resistance, and ductility.[5] Orthopedic implants must have the potential to endure load and harsh environmental conditions in the human body and integrating efficiently with adjacent bone tissue is vital for their effectiveness.[6,7]

Still, the only problem is it is susceptible to corrosion after implanting in the human body after some time which can lead to implant failure.[8] This problem could be tackled by coating

[a]*Department of Materials Science and Engineering, Ghulam Ishaq Khan (GIK) Institute of Engineering Sciences and Technology, Topi, 23640, Pakistan. E-mail: mohsin.ali@giki.edu.pk; Fax: +92-938-281032; Tel: +92-938-281026*

[b]*Materials Engineering Research Institute, Sheffield Hallam University, Sheffield, UK*

[c]*Skolkovo Institute of Science and Technology, Moscow, Russia*

[d]*Energy, Water, and Environment Lab, College of Humanities and Sciences, Prince Sultan University, Riyadh, 11586, Saudi Arabia*

[e]*Department of Mechanical Engineering, College of Engineering, Taif University, Kingdom of Saudi Arabia*

† Equal contribution.

the substrate surface with a protective film of biomaterials. Numerous investigations have been conducted to enhance the biocompatibility of implants, ensuring their acceptance by the biological system in physiological settings. Implants with bioactive coatings are useful in achieving these goals. Biocompatible materials like biopolymers (such as chitosan, alginate, and polyvinyl alcohol; PVA) and bioceramics (such as bioactive glass) are preferable for coatings on implants.[2] There are different methods to develop protective multifunctional coatings on bone implants like pulsed laser deposition, and magnetron sputtering, but electrophoretic deposition is proven to be an excellent electrochemical technique for depositing biomaterials with controlling accuracy over the deposition of functional coatings while being simple, environment-friendly, versatile and cost-effective.[2,9] Through EPD the incorporation of nanorods and bioactive substances into coatings is possible using an electric field. Due to this desired properties of coatings like high mechanical strength, biocompatibility, and antibacterial activity can be achieved.[10]

The addition of a polymer phase to a bioceramic increases the coating-substrate bonding. Polymer-based coatings like polyethylene glycol, polyvinyl alcohol, and chitosan are observed to be effective as bioactive and antimicrobial coatings and can develop biological fixation of metallic implants with the cellular matrix by enhancing cell interaction and providing support to formed tissues.[11] Also, the use of nanostructures in coatings on metallic bone implants enhances osteointegration by mimicking the bone environment more closely promoting better cell adhesion, proliferation, and differentiation. Besides this, they inhibit bacterial colonization and biofilm formation. Vera Alexandra Spirescu *et al.* developed biofilm-resistant coatings using zinc oxide (ZnO) nanoparticles with linalool.[12] Ehsan Vafa *et al.* reported a significant increase in bioactivity and enhanced osteoblast performance and proliferation through the development of a highly perforated layer of PVA, natural chitosan, and bioactive glass composite coating on 316L SS.[2] The use of natural herbs in the polymer coating can significantly enhance their functionality as a protective coating due to the presence of bioactive compounds. Liang-Liang Li *et al.* reported the use of gentamicin-loaded coating on titanium implants prepared using the electrospinning technique to provide slow drug release while exhibiting antibacterial efficacy[13] (Table 1).

In this research, we aimed to design a novel coating film to enhance the properties of a substrate.[18] Our focus was to select some novel combination of materials with easy availability, processing method, and cost-effectiveness that could enhance the properties of the substrate like biocompatibility, bioactivity, and antibacterial activity, and to provide more sites for the osteoblasts to attach at the substrate surface which leads us towards the deposition of PVA, C–H NRs, and moringa leaf extracts composite coating *via* EPD due to their significant properties required for orthopedic implant applications.[19] Bioactive materials promote cell adhesion, proliferation, and differentiation, which leads to the long-term success of the implants, reducing the risk of infections and implant failure. PVA coatings are synthetic biopolymers and can integrate well with the surrounding bone tissues and provide improved biomechanical properties, drug delivery, corrosion protection, reduced friction, and surface modification which are essential for orthopedic implants.[20] Moreover, C–H NRs help to support the coating structure and promote osteointegration, while PVA acts as a matrix for encapsulating NRs and bioactive compounds.[21] Synthesized C–H NRs offer several advantages.[22] Their nanostructure enhances surface properties and reduces the risks of implant rejection because of their excellent response against bacterial film formation. They possess excellent biocompatibility, bioactivity, and antibacterial properties which help to minimize the adverse reactions of tissues.[23] Their ability to control the release of therapeutic ions and to minimize

Table 1 An overview of similar studies to design protective coatings for the 316L SS implants

Authors	Coating materials	Coating techniques	Conclusions	Ref.
Qiang Chen *et al.*	PVA-reinforced alginate-bioglass composite coatings deposited on SS	EPD	The authors propose that the addition of PVA improved the adhesion strength and reduced the decomposition rate of the coatings, while also enhancing their hydroxyapatite-forming ability in simulated body fluid	14
I. Mendolia *et al.*	Calcium phosphate/chitosan/collagen composite coating on AISI 304 SS	Galvanic deposition	The coatings were able to slow down the corrosion of the underlying metal substrate in simulated body fluid. The coatings were found to be biocompatible based on cytotoxicity tests with pre-osteoblast cells	15
Nida Iqbal *et al.*	PVA-coated hydroxyapatite (HA) on 316L SS	EPD	The technique used by the authors to coat bioceramics onto metallic substrates was quick, reliable, and economical. The addition of 5% PVA to HA powder increased the powder's adherence to the substrate, removing the requirement for the coated substrate to be heat-treated	16
Riaz Hussain *et al.*	Mesoporous PVA/HA composites on 316L SS	EPD	An effective *in situ* synthesis of PVAHA composites is reported in the study. According to the EPD results, adding PVA enhanced coating adherence	17

the risk of infections helps to promote bone regeneration by capturing osteoblasts in their like structure which can enhance bone regeneration.[24] Additionally, their high surface area and rod-like structure enable efficient binding of proteins with the implant's surface, ensuring long-term stability.[25]

Incorporating moringa extracts has several advantages in orthopedic applications because of their antioxidant and anti-inflammatory properties and the presence of an array of phytochemicals, carotenoids, and glucosinolates.[26] Its bioactive compounds include minerals, antioxidants, anti-inflammatory substances, and wound-healing capacity, which is essential for osteogenic induction at the surface of orthopedic implants.[27] The above-mentioned properties help the implants to reduce inflammation, prevent infections and oxidative stress, and accelerate the wound-healing process to regenerate the bone.[28]

A homogeneous suspension of all these materials was prepared, and a uniform composite coating was deposited on the SS substrate using electrophoretic deposition. Through comprehensive characterization and evaluation, we were able to know that the synthesized C–H NRs have a tobermorite rod-like crystal structure which gives a hedgehog-like structure to the 29 μm thin coated film, uniformly deposited onto the SS substrate.[29,30] The designed composite coating has a hydrophilic nature, good adhesion strength, and good surface roughness which makes it more suitable for protein attachments and cellular intake. Also, the coated film exhibits good antibacterial properties against *Escherichia coli* (*E. coli*) and *Staphylococcus aureus* (*S. aureus*) because of the incorporation of C–H NRs in the coatings which makes it suitable for orthopedic applications and to improve patient satisfaction.[31] Bioactivity is an important factor when it comes to orthopedic implants because it enables interaction of the implant surface with the surrounding bone tissues. In our study, our top-performing sample demonstrated exceptional bioactivity by forming a hydroxyapatite (HA) layer and fast degradability within 24 hours.

2. Experimental

2.1 Materials

This research is carried out on a 316L SS substrate. Materials used for composite coatings on the substrate are acetic acid purchased from VWR International S.A.S (France), ethanol purchased from Meck chemical (Darmstadt Germany), polyvinyl alcohol (PVA) from Duksan pure chemicals (Korea), moringa purchased from local market and the synthesized C–H NRs in the lab by using 98% – hexadecyltrimethylammonium bromide (CTAB), tetramethylammonium hydroxide solution (TMAOH), ammonia solution max (33% NH_3 extra pure) and calcium nitrate tetrahydrate purchased from Sigma-Aldrich.

2.2 Synthesis of calcium hydrate nanorods

C–H NRs were synthesized by modifying the Stöber method.[32] 0.56 g CTAB was dissolved in 75 mL of distilled water in a beaker at 40 °C and stirred at 300 rpm. Surfactants play an essential role in defining the crystal structure of the nanoparticles. After 30 minutes of stirring, the heating was turned off, and 1.5 mL ammonia solution was added. After 30 minutes, 3.5 mL tetramethyl ammonium hydroxide solution was added dropwise *via* burette into the solution at continuous stirring. After 30 more minutes of stirring, 3.9 g of calcium nitrate tetrahydrate ($CaNO_3 \cdot 4H_2O$) was added, and the solution was left to stir for 3–4 hours at 700 rpm. After 3 hours of stirring, the solution was centrifuged at 6000 rpm for 10 minutes to collect nanorods. After collecting nanorods, washing was done two times with ethanol and distilled water and then kept for drying in the incubator at 80 °C for 24 hours. After drying, C–H NRs were collected, as shown in Fig. 1.

2.3 Suspension preparation

For electrophoretic deposition of composite coatings, 50 mL suspension with pH 3 was prepared with 6 grams per Litter concentration of solutes, including C–H NRs, PVA, and moringa herb, which needs to be deposited on the substrate as described in Fig. 1. 2 g PVA was added to the 5 mL distilled water at 80 °C and 500 rpm of stirring. After 15 minutes, the heating was turned off, and then PVA was treated slowly by adding dropwise 10 mL of acetic acid to the solution with continuous stirring for 30 minutes. Solution 2 was prepared by adding 0.5 g of C–H NRs to 30 mL ethanol followed by 0.5 g of moringa after 15 minutes, on continuous stirring for 1 hour, and ultrasonication for 30 minutes. Then slowly mix both solutions on continuous stirring. After 30 minutes of stirring, the solution was ultrasonicated for 30 minutes and then again kept on stirrer for 30 minutes.

2.4 Electrophoretic deposition

After the suspension preparation, 15 cm × 5 cm thin plates of SS were cut with the shear cutter and cleaned with ethanol. Then, after drying, samples were coated through the cathodic EPD process due to its cost-effectiveness and versatility since it can be modified easily for any specific application and is a relatively simple apparatus operative at room temperature. In the EPD process, electrodes were dipped in the suspension, where SS was used as both cathode (working electrode) and anode connected with the KPS6010D Wanptek DC Power Supply. When the current was applied, powder particles suspended in the liquid medium got positively charged, attracted towards the cathode, and deposited on the SS sample at 3 V for 7 minutes. The yield of the deposited coating is calculated by using the following formula (Table 2).

$$\%\ \text{yield} = \frac{\text{final weight} - \text{initial weight}}{\text{initial weight}} \times 100$$

2.5 Characterization

The microscopic morphologies of the synthesized nanorods and the designed composite coatings were studied using SEM coupled with EDXs (ZEISS instrument, EVO15, United Kingdom). The elemental structure identification of nanorods was carried out using X-ray diffraction (XRD, AXRD LPD, Proto, United Kingdom). The elemental structure identification of

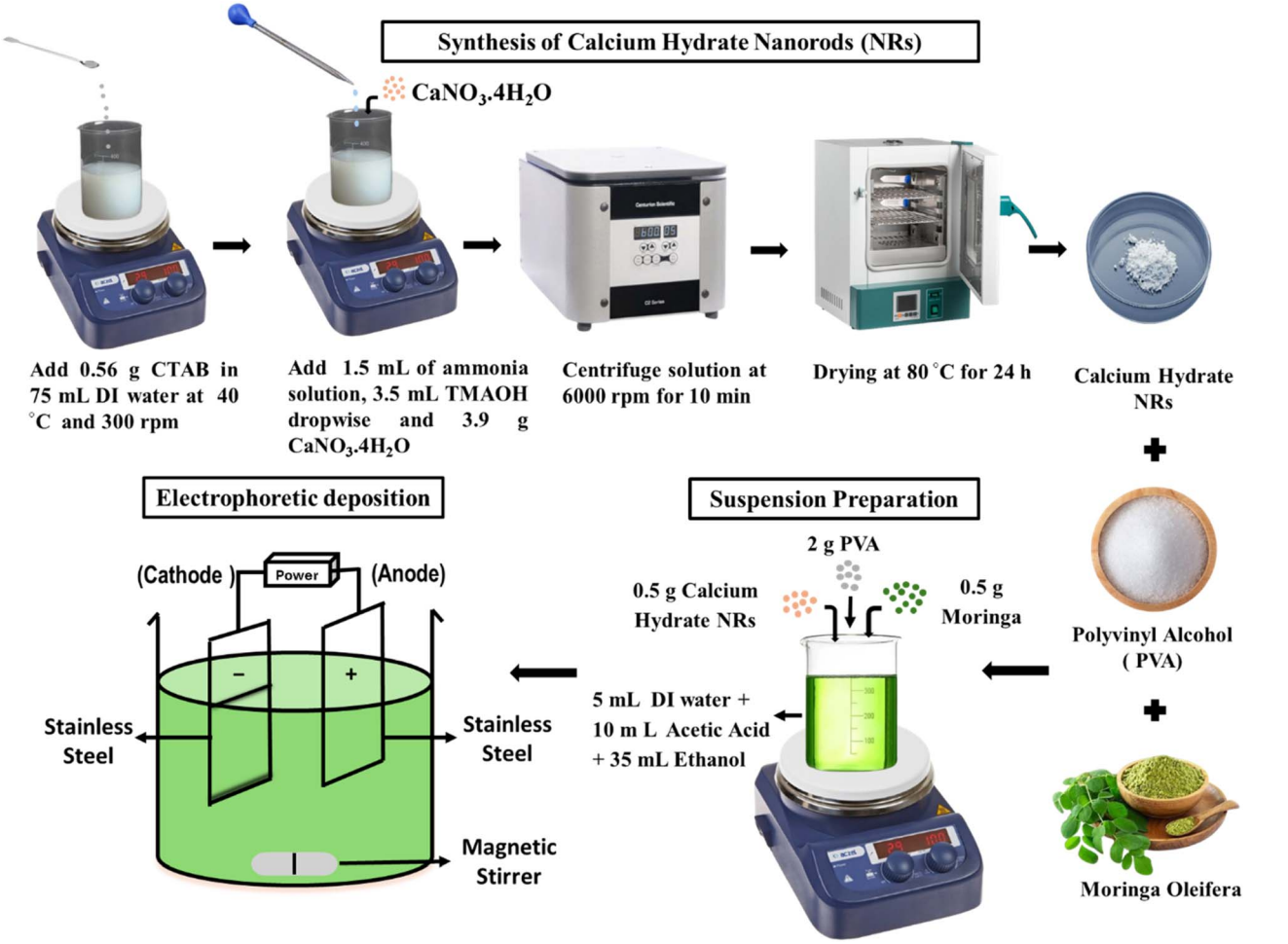

Fig. 1 Schematics for the synthesis of C–H NRs (C–H NRs) and then a suspension preparation for electrophoretic deposition by using synthesized C–H NRs along with the PVA and moringa.

Table 2 The yield of the deposited coating is listed below

Sample	Initial weight (g)	Final weight (g)	Yield (%)
Sample 1	0.376	0.382	1.59
Sample 2	0.380	0.386	1.57
Sample 3	0.369	0.375	1.63
Sample 4	0.358	0.364	1.68
Sample 5	0.361	0.367	1.66
			Average = 1.626

nanorods was carried out by recording X-ray intensity *vs.* 2-theta (2θ) using X-ray diffraction (XRD, AXRD LPD, Proto, United Kingdom) with Cu-Kα radiations over the 2θ diffraction angle ranging from 20° to 75°. To check the further chemical composition of C–H NRs, moringa, PVA, and PVA + C–H NRs + moringa composite coated substrate Fourier transformation infrared (ATR-FTIR, Thermofisher Nicolet Summit Pro) spectroscopy was performed. At first, the sample platform and knob were cleaned with 99% – ethanol properly, OMNIC paradigm software which is connected to FTIR was run and background noise was removed. After that, the sample was placed gently with the help of a spatula on the crystal of the platform and screwed down the knob right above the sample. After that sample scanning was started and recorded in the absorbance mode. The thermal analysis of polymer coating and its components is done by Simultaneous Thermal Analyzer (STA 800, PerkinElmer, USA) to analyze their thermal stability, glass transition temperature, and phase transition through endothermic peaks and corresponding weight loss curves. The composite coating analysis reveals information about its composition, verifying the presence of PVA and *Moringa oleifera* in the coating while substantiating the presence of C–H NRs as confirmed by XRD.

Surface roughness/symmetry of the deposited materials on the substrate was studied using atomic force microscopy (AFM, C3000, Nano Surf, Switzerland) in a noncontact mode using a silicon SPM-sensor with dimensions of 7 μm × 225 μm × 38 μm (thickness × length × width). Further to check the properties of the coated surface, a wettability test was performed by simply pouring a 5 μL drop of distilled water with the help of a microliter pipette on both bare SS substrate and PVA/C–H NRs/moringa coated substrate at different sites. After 5 seconds,

we took pictures of drops vertically, one by one, by adjusting the camera at the same level of drop and measuring the contact angle of that drop with both bare and coated surfaces using ImageJ software. To check further adhesion of coatings, a cross-cut tape test was done according to the ASTM standard number D3359 and was performed by putting the sample on some horizontal slab and then drawing cross hatch with the cutter on the coated substrate and examining under an optical microscope to check whether any particles of coatings got scratched or removed after that adhesive tape was applied on the coated surface where the crosshatch was drawn and pulled with force. After that, the sample was examined under an optical microscope to check the condition of the coating. The ASTM standard (D3359) was used to compare the adhesion strength of the coating. Disk diffusion tests were conducted to evaluate the antibacterial properties of the samples. Nutrient agar (Acumedia, UK) was prepared by dissolving 7 g of nutrient agar in 250 mL of distilled water and autoclaving it at 121 °C for 15 minutes for sterilization. Subsequently, 15 mL of agar was dispensed into each Petri dish and allowed to solidify. A 20 μL drop of bacterial culture from pathogenic bacterial strains *E. coli* and *S. aureus* (IDC, Islamabad) with OD 0.015 was evenly spread on separate agar plates with a glass spreader. Samples were then placed on the plates, sealed with plastic wrap, and incubated at 37 °C for 24 hours. Post-incubation, the results were observed. Data was evaluated statistically using one-way analysis of variance (ANOVA) at a significance level of $p < 0.05$. The results are reported as the mean ± standard deviation (SD) of the experiments performed in triplicate. To further check the bioactive nature of composite coated samples a test was carried out, for this purpose phosphate buffer slain (PBS, purchased from Sigma-Aldrich) solution was prepared with a pH of 7.41. 30 mL solution was poured into the falcon tubes and the coated samples were immersed in it and then kept in the shaking incubator (BioBase, China) at 37 °C at 80 rpm for 1 and 3 days. Initial weight of the samples for day 1 was 1.0771 g and for day 3 was 1.0709 g. After the completion of these specific days, samples were taken out, washed with distilled water, and dried, and SEM analysis was performed.

3. Results and discussion

3.1 Phase analysis

XRD was performed to observe the crystallographic nature of the C–H NRs. XRD data was used to obtain the hexagonal crystal structure of $Ca(OH)_2$ using VESTA software as shown in Fig. 2. Sharp characteristic peaks were observed at 2θ angles of 22.3°, 28.8°, 29.6°, 34.3°, 38.3°, 47.4°, 51°, 54.6°, 59.6°, 62.8°, 64.5°, and 72° as depicted in Fig. 3.[33] In the XRD pattern most of the planes (100), (101), (102), (110), (111), (200), and (201) (PDF Card No. 00-004-0733) are of hexagonal $Ca(OH)_2$ phase but some of the planes (012), (104) and (300) (PDF Card No. 00-005-0586) shows the presence of a rhombohedral calcite phase as well as reported in the literature.[34–36] The presence of (102) refers to the coexisting $Ca(OH)_2$, calcite, and orthorhombic aragonite phases, and the plane (202) points to the presence of $Ca(OH)_2$ and calcite phases respectively as shown in Fig. 3. Through the analysis of XRD data, it is confirmed that the hexagonal $Ca(OH)_2$ phase is the major phase present in the analyzed powder along with the calcite as sub-major phase.[34]

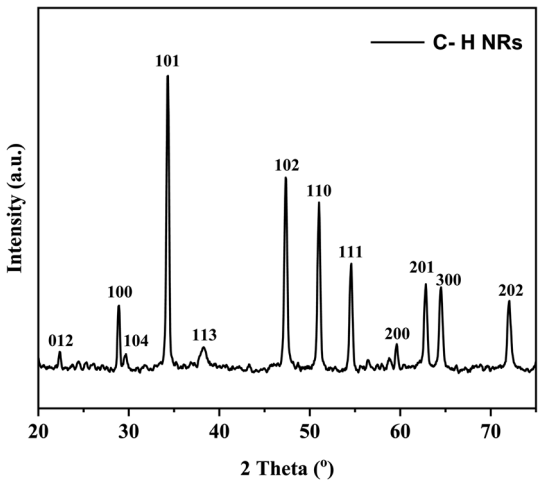

Fig. 3 X-ray diffraction of C–H NRs.

3.2 Microstructure analysis

To observe the morphology of samples, SEM along with EDS was performed. SEM analysis of C–H NRs shows an aggregated rod-like structure, as shown in Fig. 4(a1) and (a2). Most rods have a linearly elongated morphology. The size of the diameter distribution of C–H NRs is quite narrow, around 70 ± 5 nm, but the length is quite variable, which is because of the rapid nucleation time and growth rate.[37] We can achieve uniform-sized nanorods by lowering the nucleation time and growth rate which could be done by several factors, by reducing the

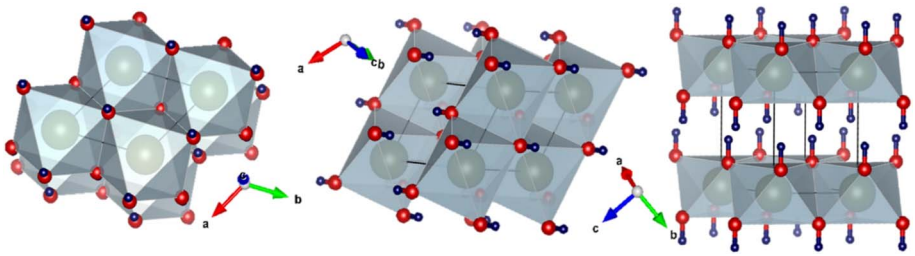

Fig. 2 Different orientations of hexagonal structure of $Ca(OH)_2$.

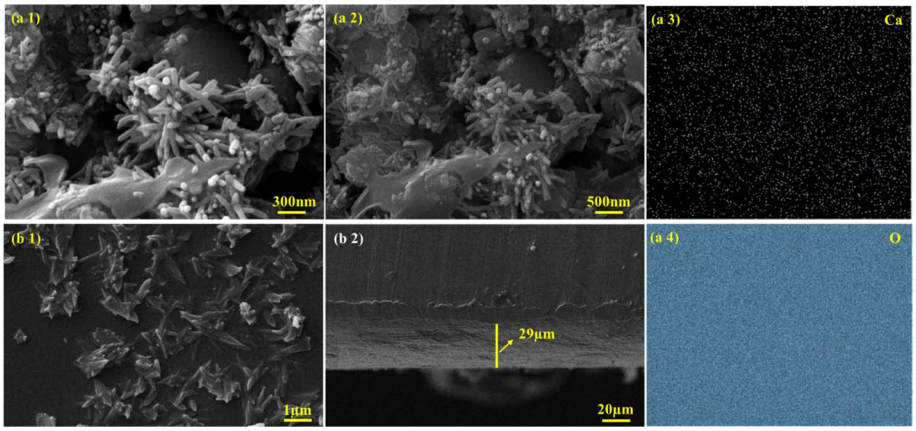

Fig. 4 Morphology of C–H NRs (a1) at 300 nm and (a2) at 500 nm. In (a3) and (a4) parts, EDS mapping of Ca, and O ions present in the C–H NRs are shown respectively. In the (b1) part, uniform deposition of the coated film is shown along with the hedgehog-like structure of C–H NRs in the coated film, and the (b2) part shows the thickness of the deposited film, which is 29 μm.

concentration of the precursors using room temperature instead of high temperature and giving more time for the synthesis of nanorods. Slower growth rates at lower temperatures facilitate the anisotropic growth with proper ultrasonication along specific crystallographic axes, promoting the formation of longer nanorods with better-defined shapes and aspect ratios.[37] Aggregation of the nanorods is because of the shorter ultrasonication time and drying time on the glass slide while preparing of sample for SEM imaging. Some 0D nanoparticles were also observed because of the improper growth of C–H NRs which could have been avoided by slower nucleation and growth rates. EDS mapping shows that calcium (Ca), and oxygen (O) are uniformly distributed all over the substrate, as shown in Fig. 4(a3) and (a4). Also, Ca and Si are observed at the same sites.

In the SEM imaging of the PVA/C–H NRs/moringa composite coated sample, a hedgehog-like structure was observed in the coated film, which is because of the incorporation of C–H NRs as seen in Fig. 4(b1) and is suitable for the osteoblasts entrapment to enhance the bone regeneration. C–H NRs are uniformly distributed all over the substrate, which may facilitate the surface area for the protein attachments. The thickness of the coated film observed is around 29 μm, which is uniform throughout the substrate, as described in Fig. 4(b2).

3.3 Fourier transformed infrared spectroscopy (FTIR) analysis

Fig. 5 shows the FTIR of PVA, moringa, C–H NRs, and composite-coated samples. A strong broader peak at 3327 cm^{-1} shows the presence of the OH group due to moisture content and alcohol. The peak at 2974 cm^{-1} shows the presence of C–H groups. A peak at 1646 cm^{-1} also shows the C–H bending in PVA, C–H NRs, and moringa while this peak of C–H bending appears later at 1717 cm^{-1} due to the native chemical environment. Also, the peak appears at 1559 cm^{-1} in both coated and C–H NRs. The peaks of C–O groups appear at 1088 cm^{-1} and 1044 cm^{-1} in all samples. The peaks at 879 cm^{-1} and 664 cm^{-1} show the presence of C=C bending and C–O bending,

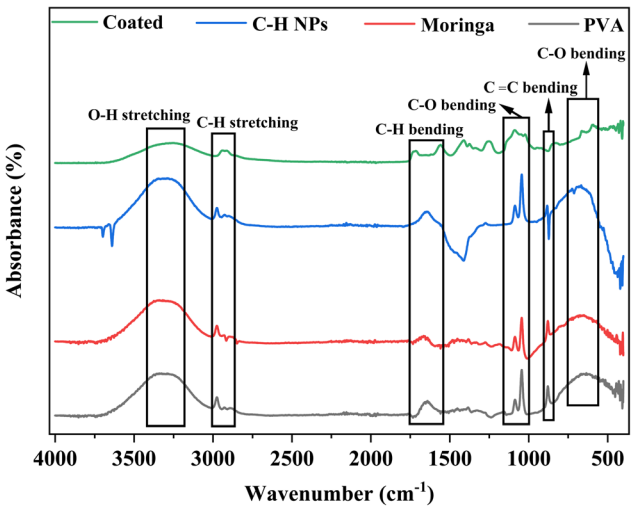

Fig. 5 FTIR of PVA, C–H NRs, moringa, and composite-coated SS substrate.

respectively. Almost all peaks of materials are aligned with the coated sample. FTIR shows all chemical bonds present in the PVA, C–H NRs, and moringa in the composite-coated sample as well which confirms the deposition of materials on the substrate.[38]

3.4 Differential scanning calorimetry and thermogravimetric analysis (DSC and TGA)

The thermal analysis is performed by TGA and DSC analyses of PVA, moringa, C–H NRs, and coating material. Due to moisture release, PVA experiences three phases of weight loss. The first stage occurs at a temperature between 45 and 1100 °C and accounts for around 5% of the total weight loss.[39] There is no discernible variation in weight loss from 110 °C. Fig. 6 demonstrates the rapid degradation of around 97% observed between the temperature range of 265 °C and 500 °C (third stage) weight loss. Both the decomposition and degradation of

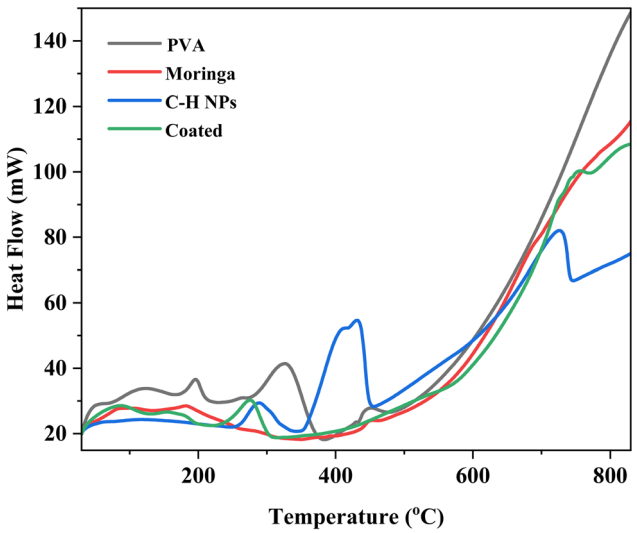

Fig. 6 DSC of PVA, C–H NRs, moringa, and composite coating material.

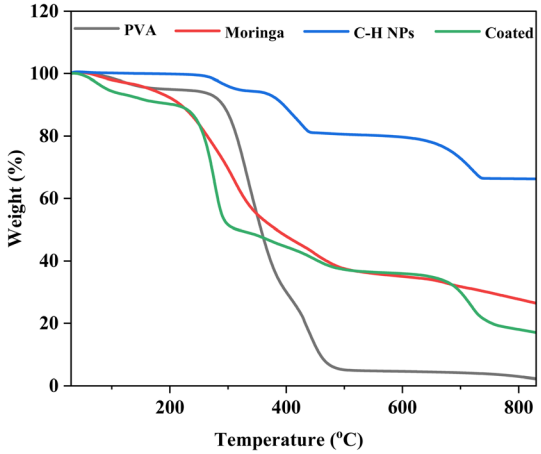

Fig. 7 TGA of PVA, C–H NRs, moringa, and composite coating material.

the PVA film are responsible for this weight loss. It can be observed that the glass transition temperature value of pure PVA film is (53.2 °C) and the melting temperature is in the range of 150–170 °C exhibiting its semi-crystalline nature. For CH-NRs, weight loss of approximately 13–17% in the temperature range of 350–500 °C due to the removal of structurally bonded water molecules whereby $Ca(OH)_2$ transforms into CaO. DSC curves exhibit well-defined endothermic peaks at 435 °C that confirm the transformation of $Ca(OH)_2$ to CaO at those respective temperatures. For moringa gum, the bonded water and free water evaporated at approximately 220–230 °C.[35,40] As evident in Fig. 7 the maximum degradation peak at 320–330 °C temperature was due to the polysaccharide chain decomposition and resulting in a residual weight of 26.28% at the end of the cycle.[41] The glass transition temperature of moringa is around 70 °C and the degradation is beginning to be observed at 185 °C. The endothermic peak was observed at corresponding temperatures which were due to the presence of an amount of moisture in the dried moringa gum and chain decomposition.[42] The coated sample exhibits much more complex thermal curves owing to the thermal stability of each of its constituents contributing to its weight loss at different temperatures and corresponding endothermic peaks during the glass transition to melting and decomposition. The glass transition temperature of the coating is 130 °C with a melting temperature of 275 °C as is evident by the prominent endothermic peak in the DSC curve. Beyond this temperature range, the decomposition of PVA and *Moringa oleifera* dominates and, the endothermic breakdown of carbon chains begins resulting in a decreasing residual mass curve that stabilizes at 800 °C at 18.2%.

3.5 Atomic force microscopy (AFM)

The AFM results of the coated substrate demonstrate a smooth surface owing to PVA while the presence of C–H NRs introduces some degrees of roughness. The coating has a Root Mean Square (RMS) roughness of 0.308 μm and an average roughness of 0.220 μm as described in Fig. 8. Since the roughness of the coating is 300 nm, it provides mechanical interlocking and wear resistance on the substrate which is essential for orthopedic applications and can provide more sites for osteoblasts attachment. The topology of the surface indicates the absence of clusters and agglomerates which demonstrates good dispersibility of constituents in the PVA matrix. The presence of ridges and valleys on the coating are observed which can be

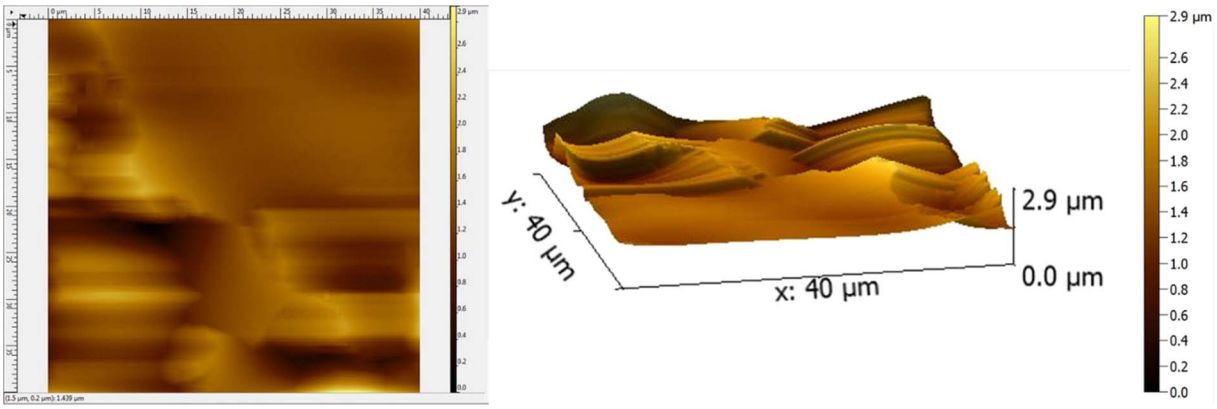

Fig. 8 AFM of the composite-coated substrate.

beneficial to the differentiation of stem cells to osteoblasts. The deposition on the surface is not uniform given the average height across is 1.348 μm. The maximum height of the deposited coating is 2.924 μm because of the presence of C–H NRs which gave a hedgehog-like structure to the coating to provide more surface area for protein attachments.

3.6 Wettability testing

A wettability test was performed on the coating to measure the contact angle to determine the hydrophilicity/hydrophobicity of the coating. ImageJ software was used to determine the contact angle. The average contact angle measured by pouring 6 DI water drops on the surface of each sample was 81 ± 1° for bare SS and 64 ± 5° for PVA, C–H NRs, and moringa composite coated sample shown in Fig. 9. It predicts that the coating was hydrophilic which is because of the presence of a huge amount of PVA in the deposited coating. The wettability of surfaces can affect surface protein adsorption and cell adhesion. According to previous studies, cells are more likely to adhere to hydrophilic surfaces.[43] The adhesion of osteoblasts decreases when the contact angle increases. When the contact angle is between 60° and 80°, the adhesion of osteoblasts is the highest.[43] That means PVA/C–H/moringa-designed coatings are suitable for cell adhesion and can enhance osteoblast attachment.

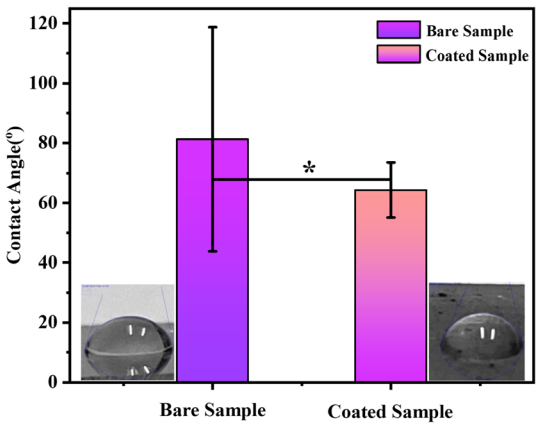

Fig. 9 Contact angle measured for both; bare stainless-steel sample and composite coated sample. The difference in the wettability value of both samples is significant (*) at $p < 0.05$.

3.7 Adhesion testing

To check the adhesion of coatings, a cross-cut tape test was done and examined under the microscope to examine if any particles got scratched or removed from the coating. On the examination, it was figured out that no coatings were removed, as shown in Fig. 10(a1) and (a2). After that, adhesive tape was applied on the coated surface, where a cross-hatch was drawn. An adhesive tape was applied to it and pulled with force. The sample was again observed under the optical microscope for any detached coating. As shown in Fig. 10(b1) and (b2), the minute amount of coating was damaged. Thus, the coating was labeled as 4B according to the ASTM standard because the damage to the coating was less than 5% which tells us that the uniformly deposited composite film of PVA, C–H NRs and moringa has good adhesion strength and has the potential of bearing harsh physiological environment of the human body and the friction produced between the body fluids and bones.

3.8 Antibacterial testing

A disk diffusion test was conducted to evaluate the antibacterial properties of the samples. The test was performed on C–H NRs and coated SS samples against two Gram-positive and Gram-

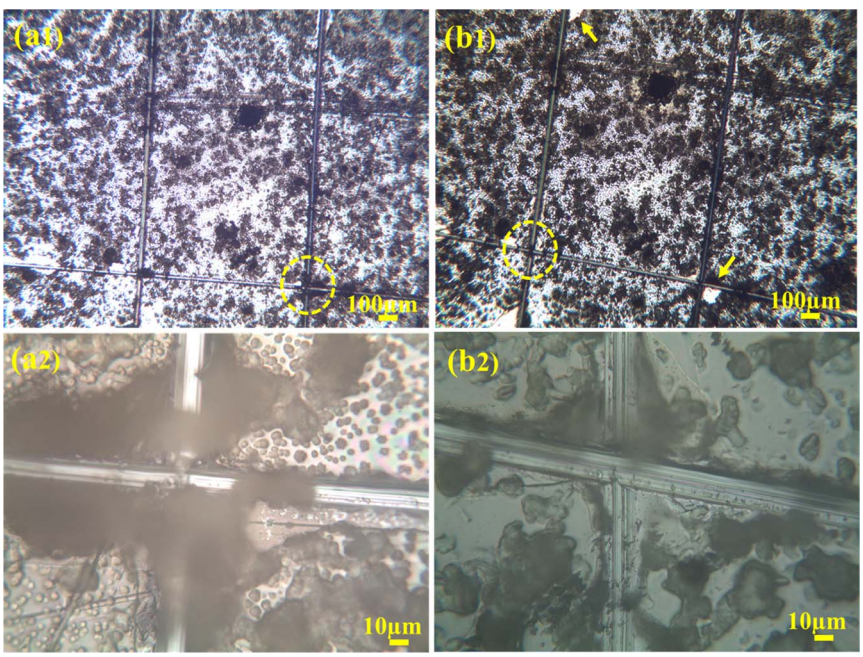

Fig. 10 Crosshatch test (a1) and (a2) encircled areas are before the adhesive tape was applied (b1) and (b2) after the tape was applied.

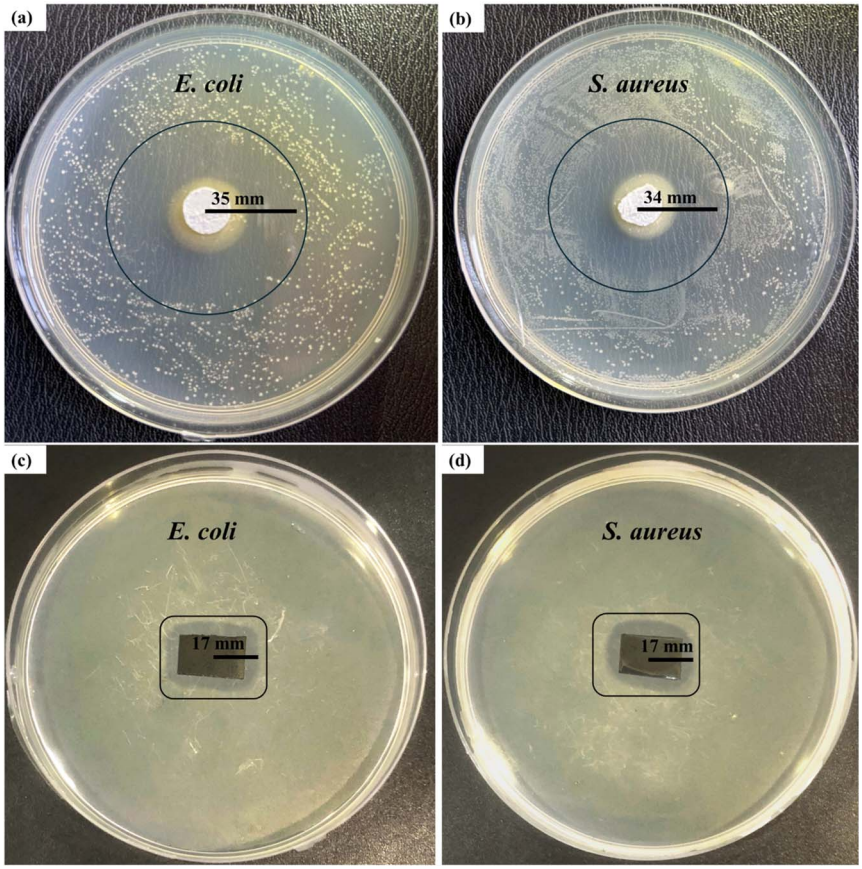

Fig. 11 Antibacterial testing of the C–H NRs against (a) *E. coli* and (b) *S. aureus*, and the coated sample against (c) *E. coli* and (d) *S. aureus* bacterial strains.

negative pathogenic bacterial strains, which are *S. aureus* and *E. coli*. A zone of inhibition of 35 ± 0.3 mm was formed against *E. coli* and 34 ± 0.6 mm against *S. aureus* was formed around the pallets of C–H NRs as shown in Fig. 11(a) and (b), confirming the good antibacterial effect of the C–H NRs which is mostly due to the high alkalinity of the nanorods. The PVA, C–H NRs, and moringa composite coated sample also inhibited the bacterial growth around the sample up to 17 ± 0.3 mm against *E. coli* and 17 ± 0.5 mm against *S. aureus* bacterial strains as shown in Fig. 11(c) & (d) which is because of the C–H NRs presence in the composite coated materials. Statistical analysis of data is presented in Fig. 12. That means the deposition of a thin layer of the designed composite coatings can prevent both Gram-positive and Gram-negative biofilm formation within the range of 17 mm of the coated substrate.

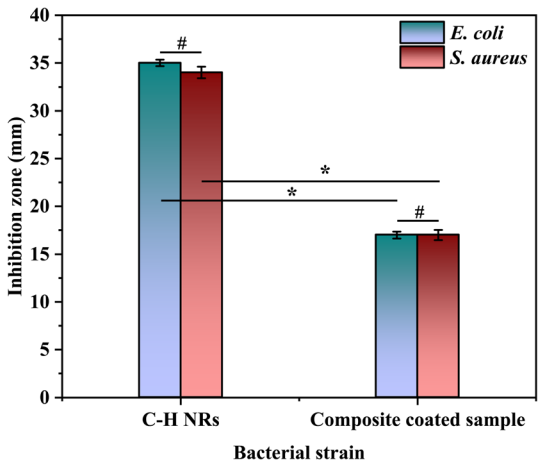

Fig. 12 Statistical analysis (ANOVA at $p < 0.05$) of antibacterial activity of SS and composite coating against *E. coli* and *S. aureus*. The SS sample and coatings showed insignificant differences (#) against both strains themselves, whereas a significant difference (*) in antibacterial effect was observed between a bare sample and coated samples in the case of each strain.

3.9 Bioactivity and degradability testing

The bioactivity of the coated samples measured in the PBS showed excellent results. The morphology of the coated sample changed after the immersion of samples in PBS even after day 1 and confirmed the formation of a flower-like structure as shown in Fig. 13, because of the presence of calcium phosphate (Ca–P) layer which is essential for the attachment of osteoblasts. The chemical composition of the layer is evaluated through EDX and used to calculate the Ca/P ratio of the formed hydroxyapatite (HA) layer. The calculated ratio of Ca/P was 0.63 ± 0.2 which indicates that the formed layer of hydroxyapatite is calcium

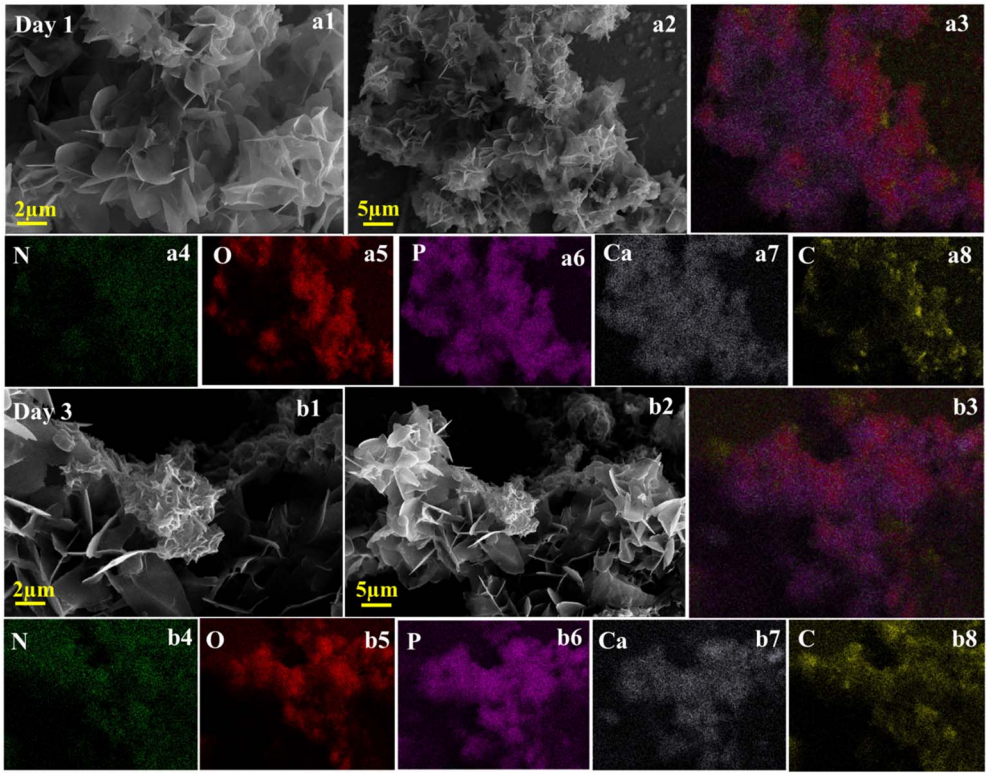

Fig. 13 SEM images shows the formation of HA layer after day 1 (a1 and a2) and day 3 (b1 and b2) after the immersion of coated samples in PBS and the elemental analysis of samples confirms the presence of Ca and P along with O, N, C elements as shown in (a3–a8 and b3–b8).

deficient which is possibly because of the low release of Ca ions. Further, the formation of the HA layer is also confirmed from the XRD data as shown in Fig. 14. The diffraction pattern showed peaks associated with HA at 31.7° (211) and 46° (222) for both samples (JCPDS Card#9-0432). The development of the HA layer on the composite coatings highlights the implant's ability to form a bond with the natural bone material. Moreover, the intensity of peaks at 31.7° for the day 3 sample is higher than for the day 1 sample which is due to the increased amount of HA formation on the coating. Henceforth, composite coatings not only bond well to HA but also promote its growth.[44] The degradability of coatings is depicted in Fig. 15 in PBS. The average % yield obtained from the deposited coating was 1.626%. When the samples were immersed in PBS, the samples exhibited a weight loss of 0.576% on day 1 while on day 3, they displayed a weight loss of 0.674% of the deposited coating. The degradability of coatings shows a significant difference between day 1 and day 3 while the difference of degradability is

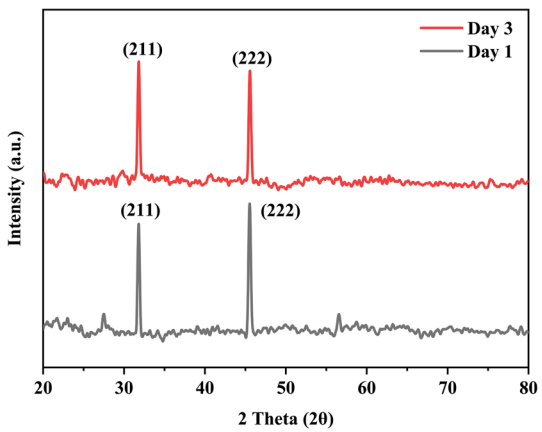

Fig. 14 XRD graph of samples with HA layer formation on day 1 and day 3 after the immersion of samples in PBS.

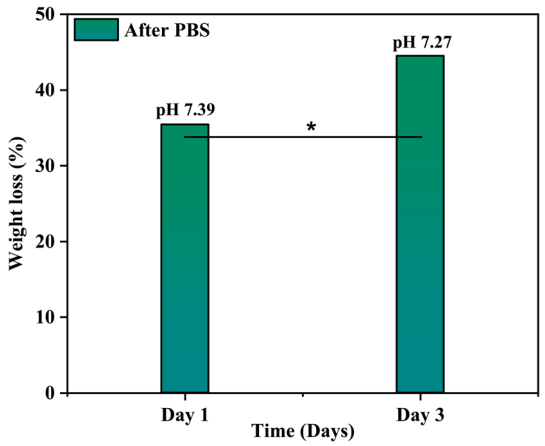

Fig. 15 Statistical analysis (ANOVA $p < 0.05$) of degradability of composite coatings in PBS at 7.41 pH. The difference between the degradability of coatings is significant (*) between day 1 and day 3.

insignificant between the sample before and after PBS immersion. 35.4% of the coating was degraded on day 1 while 44.5% of the coating was degraded on day 3. This might be because of the permeation of the medium into the pores due to which coatings have shown fast degradation.[45]

4. Conclusion

The development of composite coatings represents a significant advancement in addressing the limitations of metals in bone implants. Even though metals offer strength and load-bearing capabilities, they are prone to corrosion and biofilm formation and require enhanced biocompatibility, bioactivity, and antibacterial effects to be used for orthopedic implants. By creating composite coatings with polyvinyl alcohol, C–H NRs, and moringa, this study addressed these issues. These coatings were effectively applied to 316L SS using electrophoretic deposition, enhancing fibroblast attachment and antibacterial protection. Scanning electron microscopy and X-ray diffraction verified the intended shape and crystal structure of nanorods and coated film. FTIR confirms the chemical composition of selected materials onto the coated substrate. AFM, wettability, and cross-hatch adhesion test revealed good surface roughness, hydrophilicity, and higher adhesion strength of the deposited coating on the substrate, which provided sites for the osteoblast settlement. In addition, the DSC and TGA results revealed enhanced thermal stability of the material of interest by incorporating C–H NRs. Moreover, the coatings showed remarkable antibacterial activity against Gram-positive and Gram-negative bacteria, a good hydrophilic nature for protein attachment, and reliable adhesion due to incorporating C–H NRs. Moreover, the sample of interest demonstrated exceptional bioactivity by forming a hydroxyapatite (HA) layer within 24 hours, with fast degradability of 35.4% within 24 hours and 44.5% in 48 hours. These results highlight the composite film's potential to provide an affordable solution while improving the biocompatibility, bioactivity, and antibacterial qualities of orthopedic implants made of SS.

Data availability

The data that supports the findings of this study are available with the first author upon reasonable request.

Conflicts of interest

The authors declare that they have no known competing financial interests or personal relationships that could have appeared to influence the work reported in this paper.

Acknowledgements

M. A. Marwat acknowledges the valuable academic and research support from Ghulam Ishaq Khan (GIK) Institute of Engineering Sciences and Technology. The authors would like to acknowledge Prince Sultan University Riyadh Saudi Arabia. The authors would like to acknowledge the Deanship of Graduate Studies and Scientific Research, Taif University, for funding this work.

References

1 M. L. Terranova, Key challenges in diamond coating of titanium implants: Current status and future prospects, *Biomedicines*, 2022, **10**(12), 3149.
2 E. Vafa, R. Bazargan-Lari and M. E. Bahrololoom, Electrophoretic deposition of polyvinyl alcohol/natural chitosan/bioactive glass composite coatings on 316L stainless steel for biomedical application, *Prog. Org. Coat.*, 2021, **151**, 106059.
3 R. A. Gittens, R. Olivares-Navarrete, A. Cheng, D. M. Anderson, T. McLachlan, I. Stephan, *et al.*, The roles of titanium surface micro/nanotopography and wettability on the differential response of human osteoblast lineage cells, *Acta Biomater.*, 2013, **9**(4), 6268–6277.
4 A. Nouri and C. Wen, 3 – Stainless steels in orthopedics, in *Structural Biomaterials*, ed. Wen C., Woodhead Publishing, 2021, pp. 67–101.
5 A. A. Zadpoor, Additively manufactured porous metallic biomaterials, *J. Mater. Chem. B*, 2019, **7**(26), 4088–4117.
6 D. Pathote, D. Jaiswal, V. Singh and C. K. Behera, Optimization of electrochemical corrosion behavior of 316L stainless steel as an effective biomaterial for orthopedic applications, *Mater. Today: Proc.*, 2022, **57**, 265–269.
7 N. E. Putra, M. J. Mirzaali, I. Apachitei, J. Zhou and A. A. Zadpoor, Multi-material additive manufacturing technologies for Ti-, Mg-, and Fe-based biomaterials for bone substitution, *Acta Biomater.*, 2020, **109**, 1–20.
8 U. K. Mudali, T. Sridhar, N. Eliaz and B. Raj, Failures of Stainless Steel Orthopedic Devices – Causes and Remedies, *Corros. Rev.*, 2003, **21**, 231–267.
9 A. W. Bridges and A. J. García, Anti-inflammatory polymeric coatings for implantable biomaterials and devices, *J. Diabetes Sci. Technol.*, 2008, **2**(6), 984–994.
10 M. N. Abdallah, *Evaluation of a Novel Anabolic Bone Drug with Synthetic Bone Graft Biomaterials in a Rat Jaw Bone Defect*, University of Toronto, Canada, 2020.
11 J. Adhikari, P. Saha and A. Sinha, Surface modification of metallic bone implants—Polymer and polymer-assisted coating for bone in-growth, in *Fundamental Biomaterials: Metals*, ed. Balakrishnan P., Sreekala M. S. and Thomas S., Woodhead Publishing, 2018, pp. 299–321.
12 V. A. Spirescu, R. Șuhan, A. G. Niculescu, V. Grumezescu, I. Negut, A. M. Holban, *et al.*, Biofilm-Resistant Nanocoatings Based on ZnO Nanoparticles and Linalool, *Nanomaterials*, 2021, **11**(10), 2564.
13 L.-L. Li, L.-M. Wang, Y. Xu and L.-X. Lv, Preparation of gentamicin-loaded electrospun coating on titanium implants and a study of their properties in vitro, *Arch. Orthop. Trauma Surg.*, 2012, **132**(6), 897–903.
14 Q. Chen, S. Cabanas-Polo, O.-M. Goudouri and A. R. Boccaccini, Electrophoretic co-deposition of polyvinyl alcohol (PVA) reinforced alginate–Bioglass® composite

coating on stainless steel: Mechanical properties and in-vitro bioactivity assessment, *Mater. Sci. Eng., C*, 2014, **40**, 55–64.

15 I. Mendolia, C. Zanca, F. Ganci, G. Conoscenti, F. C. Pavia, V. Brucato, *et al.*, Calcium phosphate/polyvinyl acetate coatings on SS304 via galvanic co-deposition for orthopedic implant applications, *Surf. Coat. Technol.*, 2021, **408**, 126771.

16 N. Iqbal, R. Nazir, A. Asif, A. A. Chaudhry, M. Akram, G. Y. Fan, *et al.*, Electrophoretic deposition of PVA coated hydroxyapatite on 316L stainless steel, *Curr. Appl. Phys.*, 2012, **12**(3), 755–759.

17 R. Hussain, S. Tabassum, M. A. Gilani, E. Ahmed, A. Sharif, F. Manzoor, *et al.*, In situ synthesis of mesoporous polyvinyl alcohol/hydroxyapatite composites for better biomedical coating adhesion, *Appl. Surf. Sci.*, 2016, **364**, 117–123.

18 M. Djošić, A. Janković, M. Stevanović, J. Stojanović, M. Vukašinović-Sekulić, V. Kojić, *et al.*, Hydroxyapatite/poly(vinyl alcohol)/chitosan coating with gentamicin for orthopedic implants, *Mater. Chem. Phys.*, 2023, **303**, 127766.

19 M. I. Baker, S. P. Walsh, Z. Schwartz and B. D. Boyan, A review of polyvinyl alcohol and its uses in cartilage and orthopedic applications, *J. Biomed. Mater. Res., Part B*, 2012, **100**(5), 1451–1457.

20 M. Kobayashi and H. S. Hyu, Development and evaluation of polyvinyl alcohol-hydrogels as an artificial articular cartilage for orthopedic implants, *Materials*, 2010, **3**(4), 2753–2771.

21 A. Harugade, A. P. Sherje and A. Pethe, Chitosan: a review on properties, biological activities and recent progress in biomedical applications, *React. Funct. Polym.*, 2023, **191**, 105634.

22 Y. AlNatheer, S. Devanesan, O. G. Alghamdi, M. S. AlSalhi and S. A. Seif, Calcium hydroxide nanoparticles synthesized with medicinal plants extract as surface coating for titanium alloy bone implants using a simple method: characterization and biomechanical evaluation, *Biocatal. Agric. Biotechnol.*, 2024, **58**, 103165.

23 J. Wu, Y.-J. Zhu, F. Chen, X.-Y. Zhao, J. Zhao and C. Qi, Amorphous calcium silicate hydrate/block copolymer hybrid nanoparticles: synthesis and application as drug carriers, *Dalton Trans.*, 2013, **42**(19), 7032–7040.

24 R. V. R. Virtudazo, H. Watanabe, T. Shirai and M. Fuji, Simple preparation and initial characterization of semi-amorphous hollow calcium silicate hydrate nanoparticles by ammonia-hydrothermal-template techniques, *J. Nanopart. Res.*, 2013, **15**, 1–9.

25 R. Maddalena, K. Li, P. A. Chater, S. Michalik and A. Hamilton, Direct synthesis of a solid calcium-silicate-hydrate (C-S-H), *Constr. Build. Mater.*, 2019, **223**, 554–565.

26 A. Chiş, P. A. Noubissi, O.-L. Pop, C. I. Mureşan, M. A. Fokam Tagne, R. Kamgang, *et al.*, Bioactive compounds in Moringa oleifera: mechanisms of action, focus on their anti-inflammatory properties, *Plants*, 2023, **13**(1), 20.

27 S. E. Agarry, K. M. Oghenejoboh, O. A. Aworanti and A. O. Arinkoola, Biocorrosion inhibition of mild steel in crude oil-water environment using extracts of Musa paradisiaca peels, Moringa oleifera leaves, and Carica papaya peels as biocidal-green inhibitors: kinetics and adsorption studies, *Chem. Eng. Commun.*, 2019, **206**(1), 98–124.

28 L. Gopalakrishnan, K. Doriya and D. S. Kumar, Moringa oleifera: A review on nutritive importance and its medicinal application, *Food Sci. Hum. Wellness*, 2016, **5**(2), 49–56.

29 W. Wei, W. Song and S. Zhang, Preparation and Characterization of Hydroxyapatite-Poly (Vinyl Alcohol) Composites Reinforced with Cellulose Nanocrystals, *BioResources*, 2014, **9**(4), 6087–6099.

30 R. Barberi, J. J. Bonvent, R. Bartolino, J. Roeraade, L. Capelli and P. G. Righetti, Probing soft polymeric coatings of a capillary by atomic force microscopy, *J. Chromatogr. B: Biomed. Sci. Appl.*, 1996, **683**(1), 3–13.

31 K. A. Kravanja and M. Finšgar, Analytical techniques for the characterization of bioactive coatings for orthopaedic implants, *Biomedicines*, 2021, **9**(12), 1936.

32 M. Monasterio, J. J. Gaitero, E. Erkizia, A. M. Guerrero Bustos, L. A. Miccio, J. S. Dolado, *et al.*, Effect of addition of silica- and amine functionalized silica-nanoparticles on the microstructure of calcium silicate hydrate (C–S–H) gel, *J. Colloid Interface Sci.*, 2015, **450**, 109–118.

33 A. Verganelaki, C. Kapridaki and P. Maravelaki-Kalaitzaki, Modified Tetraethoxysilane with Nanocalcium Oxalate in One-Pot Synthesis for Protection of Building Materials, *Ind. Eng. Chem. Res.*, 2015, **54**(29), 7195–7206.

34 A. Samanta, D. K. Chanda, P. S. Das, J. Ghosh, A. K. Mukhopadhyay and A. Dey, Synthesis of nano calcium hydroxide in aqueous medium, *J. Am. Ceram. Soc.*, 2016, **99**(3), 787–795.

35 Harish, P. Kumar, B. Malhotra, P. Phalswal, P. K. Khanna, A. Salim, *et al.*, Effect of reaction rate on the properties of chemically synthesized calcium hydroxide nanoparticles, *Mater. Today: Proc.*, 2020, **28**, 2305–2310.

36 C. Rodriguez-Navarro, A. Suzuki and E. Ruiz-Agudo, Alcohol Dispersions of Calcium Hydroxide Nanoparticles for Stone Conservation, *Langmuir*, 2013, **29**(36), 11457–11470.

37 B. Wiley, Y. Sun and Y. Xia, Synthesis of silver nanostructures with controlled shapes and properties, *Acc. Chem. Res.*, 2007, **40**(10), 1067–1076.

38 D. L. Pavia, G. M. Lampman, G. S. Kriz and J. R. Vyvyan, *Introduction to Spectroscopy*, 2015.

39 O. W. Guirguis and M. T. H. Moselhey, *Thermal and Structural Studies of Poly (Vinyl Alcohol) and Hydroxypropyl Cellulose Blends*, 2011.

40 V. P. Jadhav, C. T. Chakraborty and D. M. Nerkar, *Nanoparticle-Embedded Polymer: Preparation and Characterization of PVA-PPy-Au Nanocomposite Free Standing Films*, 2018, pp. 136–147.

41 P. Liu, W. Chen, Y. Liu, S. Bai and Q. Wang, Thermal melt processing to prepare halogen-free flame retardant poly(vinyl alcohol), *Polym. Degrad. Stab.*, 2014, **109**, 261–269.

42 R. Koley, R. Kasilingam, S. Sahoo, S. Chattopadhyay and A. K. Bhowmick, Synthesis and Characterization of Phenol Furfural Resin from Moringa Oleifera Gum and Biophenol

and Its Application in Styrene Butadiene Rubber, *Ind. Eng. Chem. Res.*, 2019, **58**(40), 18519–18532.

43 L.-C. Xu and C. A. Siedlecki, Effects of surface wettability and contact time on protein adhesion to biomaterial surfaces, *Biomaterials*, 2007, **28**(22), 3273–3283.

44 J. Manzur, M. Akhtar, A. Aizaz, K. Ahmad, M. Yasir, B. Z. Minhas, *et al.*, Electrophoretic Deposition, Microstructure, and Selected Properties of Poly(lactic-co-glycolic) Acid-Based Antibacterial Coatings on Mg Substrate, *ACS Omega*, 2023, **8**(20), 18074–18089.

45 S. Alamri, N. A. Nafady, A. M. El-Sagheer, M. A. El-Aal, Y. S. Mostafa, M. Hashem, *et al.*, Current Utility of Arbuscular Mycorrhizal Fungi and Hydroxyapatite Nanoparticles in Suppression of Tomato Root-Knot Nematode, *Agronomy*, 2022, **12**(3), 671.